JGR Solid Earth

RESEARCH ARTICLE
10.1029/2019JB017788

Lithospheric SH Wave Velocity Structure Beneath the Northeastern Tibetan Plateau From Love Wave Tomography

Yuanyuan V. Fu[1], **Lun Li**[2,3], **and Zhuo Xiao**[4]

[1]Key Laboratory of Earthquake Prediction, Institute of Earthquake Forecasting, China Earthquake Administration, Beijing, China, [2]Guangdong Provincial Key Lab of Geodynamics and Geohazards, School of Earth Sciences and Engineering, Sun Yat-sen University, Guangzhou, China, [3]Southern Marine Science and Engineering Guangdong Laboratory (Zhuhai), Zhuhai, China, [4]Guangzhou Institute of Geochemistry, Chinese Academy of Sciences, Guangzhou, Guangdong, China

Key Points:
- Prominent slow SH wave velocity is observed in the midlower crust of NE Tibet, probably implying the existence of partial melting
- The high topography of the northeastern Tibet could result from compensations by deep-seated thermal buoyancy in the upper mantle
- The western Qinling orogen is imaged by high velocity in the entire lithosphere, ruling out the possibility of any crustal channel flow

Supporting Information:
- Supporting Information S1

Correspondence to:
L. Li,
lilun6@mail.sysu.edu.cn

Citation:
Fu, Y. V., Li, L., & Xiao, Z. (2019). Lithospheric SH wave velocity structure beneath the northeastern Tibetan plateau from Love wave tomography. *Journal of Geophysical Research: Solid Earth*, *124*, 9682–9693. https://doi.org/10.1029/2019JB017788

Received 7 APR 2019
Accepted 9 AUG 2019
Accepted article online 16 AUG 2019
Published online 10 SEP 2019

Abstract The northeastern (NE) Tibetan plateau has been a prime site to understand the dynamic processes responsible for the rise and lateral growth of the Tibetan plateau. Here we construct a high-resolution lithospheric scale isotropic SH wave velocity model (down to the depth of 130 km) for the NE Tibetan plateau and its adjacent regions based on the measurements of fundamental-mode Love wave dispersions (20–100 s) with seismic data recorded by ChinArray II and China Digital Seismic Array using two-plane wave method. Prominent slow SH wave velocity (V_{SH}) is observed in the midlower crust of the NE Tibetan plateau, specifically in the Qilian Orogenic Belt and the Songpan-Ganzi Terrane regions, coincident with previously indicated significantly slow SV wave velocity (V_{SV}), probably implying the existence of partial melts in the midlower crust. This low SH wave velocity anomaly could be traced down to the uppermost mantle, indicating a weak and warm lithosphere, which we interpret as a consequence of asthenosphere upwelling after lithospheric mantle removal in the NE Tibetan plateau. The asthenosphere upwelling and associated deep-seated thermal buoyancy could explain the occurrence of partial melting in the mid-lower crust and account for parts of high elevations in the NE Tibetan plateau. The western Qinling orogenic belt is characterized with a high velocity anomaly in most of lithosphere, which is inconsistent with the existence of channel flow within the lithosphere along the Qinling orogenic belt from the Tibetan plateau.

1. Introduction

The Cenozoic collision between the Indian and Eurasian plates has resulted in the formation of the Tibetan plateau in current stage (Beck et al., 1995; Yin & Harrison, 2000). The modern plateau is characterized by high elevation with flat-topped and steep-sided morphology (Fielding et al., 1994). Convergence and deformation continue today, but the mechanisms responsible for the plateau's uplift remain debated. Previous studies suggested that the high reliefs of the plateau could result from either a highly thickened upper crust through brittle faulting and folding (e.g., Houseman & England, 1993), ductile flow and inflation of the lower crust (e.g., Beaumont et al., 2001; Bird, 1991), deep-seated thermal buoyancy due to the delamination or convective removal of tectonically thickened lithospheric mantle (England & Houseman, 1989; Jimenez-Munt & Platt, 2006; Molnar et al., 1993), or extrusive rigid block (Tapponnier et al., 2001).

It appears that crustal isostasy dominates in the southern Tibetan plateau while thermal isostasy in the mantle works in north of the plateau, where a relatively thinner crust is observed (Jimenez-Munt et al., 2008; Tseng et al., 2009). Geophysical observations suggest that the uplift of southeast Tibetan plateau, where the crust thickens without significant upper crustal shortening (Schoenbohm et al., 2006), tends to be associated with lower crustal flow (e.g., Bai et al., 2010; Bao, Sun, et al., 2015; Hu et al., 2000; Huang et al., 2015; Xu et al., 2007). Global Positioning System measurements indicate that the northeastern (NE) Tibetan plateau, where is defined by the Haiyuan fault system in the north, the Liupan Shan in the east, the Kunlun fault system in the south, and the Altyn Tagh fault system in the west, undergoes apparent rising with typical rates between 0 and 2 mm/year (Liang et al., 2013) and active NE-SW shortening at a rate of ~13 mm/year, only slightly less than across the Himalayas (Chen et al., 2000). The question of whether upper crustal

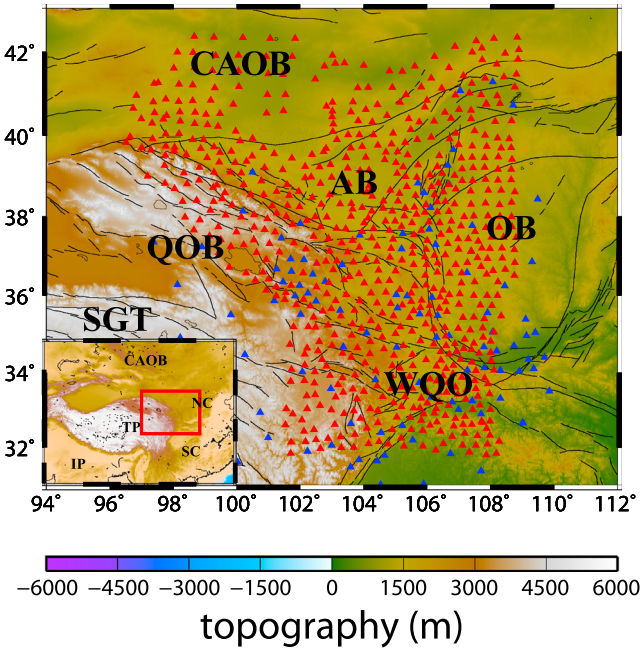

Figure 1. Tectonic map of the northeastern Tibetan plateau. Red and blue triangles represent the temporary stations from ChinArray II and permanent stations from China Digital Seismic Array, respectively. IP = Indian Plate; TP = Tibetan Plateau; SC = South China; NC = North China; CAOB = Central Asian Orogenic Belt; AB = Alxa Block; OB = Ordos Block; QOB = Qilian orogenic belt; SGT = Songpan-Ganzi terrane; WQO = Western Qinling Orogen.

thickening, the crustal flow, or mantle lithospheric dynamic process is responsible for the uplift in NE Tibetan plateau remains obscure. Clark et al. (2005) suggested the presence of crustal flow in the NE Tibetan plateau via fitting the observed northeastward sloping topography by inducing an underlying lower crustal channel with a thickness of 15 km. Recent geophysical observations offer several lines of evidence, such as low velocity zone (Bao et al., 2013; Schoenbohm et al., 2006; Yang et al., 2012) and strong radial anisotropy (Duret et al., 2010; Li et al., 2016; Shapiro et al., 2004; Xie et al., 2013) in the middle and/or lower crust, in support of the existence of crustal flow in this region. However, the low and moderate Poisson's ratio (Wang et al., 2016; Xu et al., 2013) indicated a generally felsic crust in this region, which is contradictory to the mafic crustal composition predicted by the lower crustal flow model (Pan & Niu, 2011). Additionally, large and coherent crustal seismic anisotropy from receiver function (Wang et al., 2016) is attributed to the vertical coherent shortening, contrasting to the lower crustal flow model. Moreover, some studies argue that the upper crustal shortening is sufficient to explain the current elevation of the region without an appeal for additional contributing factors such as channel flow (e.g., Gao et al., 2013; Lease et al., 2012). Recently, local or regional-scale lithospheric delamination have been invoked to explain the high elevation of NE Tibetan plateau, specifically Qilian orogenic belt (QOB) and Anyemaqen Mountain, as suggested by a low velocity anomaly in the uppermost mantle observed from a number of tomographic results (Li et al., 2013, 2016; Lei & Zhao, 2016; Li et al., 2017; Zheng et al., 2016). In fact, the removal of the mantle lithosphere has been suggested to occur beneath the whole plateau at about 8 Ma (Molnar et al., 1993), which could lead to rapid rise of the plateau (e.g., Métivier et al., 1998). However, it is not clear whether the lithospheric root is also removed in the NE Tibetan plateau.

Given above mentioned ongoing debates, in this study we construct a high-resolution SH wave velocity (V_{SH}) model from Love wave tomography based on the dense seismic array ChinArray II and the permanent China Digital Seismic Array in the NE Tibetan plateau (Figure 1). Our current high-resolution V_{SH} model could provide more details than the one obtained from previous Love wave tomography (Li et al., 2016), which has limited station coverage and covers parts of the NE Tibetan plateau, and could offer a line of additional independent evidence on the existing controversies. Our result would have important implications for understanding the dynamic processes responsible for the rise and lateral growth of the Tibetan plateau.

2. Data and Methods

We applied the modified two-plane wave method on fundamental-mode Love waves for phase velocity inversion (Li & Li, 2015). We selected earthquakes with epicentral distances between 20° and 150°, focal depth less than 200 km, and M_b larger than 5.5 (Figure 2). The transverse components of seismograms after the rotation of the north and east components were used to identify Love wave trains. The events with low signal-to-noise ratios were eliminated visually. The seismic data were recorded by the temporary ChinArray II array (650 broadband stations) and the permanent China Digital Seismic Array (102 broadband stations) that were deployed across the NE Tibetan plateau (Figure 1). The dense ChinArray II operated continuously for 2.5 years between 2013 and 2016. All instrument responses were corrected before processing. We measured Love wave phase velocities for 12 frequency bands ranging from 10 to 50 mHz and utilized 10-mHz-wide Butterworth filters centered on each frequency. In order to increase the reliability of inversions, we applied strict data selection criteria following the procedure of Li and Li (2015) and rejected the data that exhibit strong interferences from higher modes or multiple surface-reflected SH waves and inconsistency between stations due to a complicated incoming wave field. Those Love wave waveforms with good signal-to-noise ratios were chosen and isolated with a rectangular window with a cosine taper for each

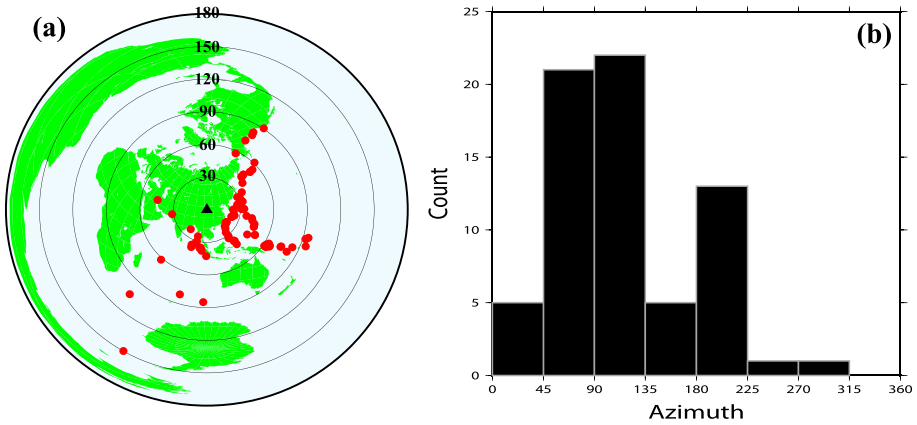

Figure 2. (a) Distribution of the teleseismic events (red circles) used in this study. The black triangle indicates the center of the seismic array. (b) Azimuth distribution of those events.

frequency. The length of window was determined based on the epicentral distance and dispersion characteristics. We kept the same window length for all seismograms for a given event (Figure 3). Sixty-eight teleseismic events were retained in this study. These events have good azimuthal coverage except in the north (Figure 2). Given the large number of stations, we can still obtain dense crossing ray paths in the NE Tibetan plateau. We measured phases and amplitudes of windowed data using Fourier analysis.

The first step in our inversion is computing isotropic phase velocities for each frequency using both amplitude and phase data of Love waves. The two plane wave parameters and phase velocities were simultaneously solved in the inversion through a standard, iterative, linearized inversion technique (Tarantola & Valette, 1982). There is a trade-off between model variance and model resolution. We used a smoothing length of 80 km to invert for the phase velocity at all periods to reduce the effects of this trade-off after testing a variety of values. A priori standard deviation of 0.25 km/s was chosen to provide light damping for the phase velocity. The standard deviation of phase velocity was calculated based on the model covariance matrix, and its distribution at each period exhibits similar patterns with small values in the interior of the study area and large errors toward the edge. Additionally, its magnitude increases with period. To increase reliability, we only interpret phase velocities with errors less than the 1% contour of twice the standard errors at 20 s. We parameterized phase velocity in the study area by a grid with intervals varying from 0.5° in the center to 0.75° at the edge. We first obtained the average phase velocity at each period. Then these average phase velocities were used as starting values in the inversion for 2-D variations of phase velocities.

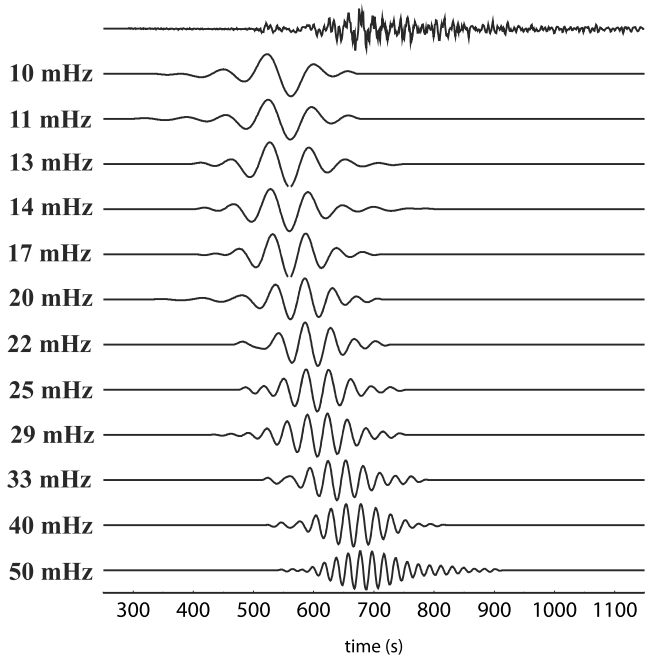

Figure 3. An example of the waveforms of the fundamental-mode Love wave at station 64052 from an intermediate depth earthquake (24.2N, 122.3E) on 20 April 2015.

The second and last step of the inversion is inverting SH wave velocities from the obtained isotropic Love wave phase velocities with the partial derivatives from Saito (1988). We modified the AK135 model with constraints from the shear velocity values in the crust and uppermost mantle from previous Rayleigh wave tomography study (Li et al., 2017). We defined 50 layers with three crustal layers from the surface to 410-km depth. The crust thickness in the study area was adapted from previous receiver function study (Wang et al., 2017) and remained unchanged during the inversion. Considering few earthquakes from northwest, we set an a priori standard error of 0.05 km/s for the shear wave velocity to balance the model resolution and oscillation after several tests. We first performed the inversion with the average Love wave phase velocity as inputs to determine 1-D average SH wave velocity in entire study area. The 3-D SH wave velocity model was constructed by assembling 1-D inversion results at each grid node.

3. Results

3.1. Resolution Tests

The accuracy of tomographic results depends on path coverage, frequency, and model parameterization of the Love wave inversion. Traditional checkerboard tests were performed to evaluate the resolution of phase velocity maps. The magnitude of the input velocity perturbation was set to 4% with a dimension of 1.5° × 1.5°. Synthetic data were calculated using the same ray paths and regularization as the real inversion. Gaussian-distributed random noise was added to synthetic phases and amplitudes based on the noise level in the real data. Inversion results obtained from noisy synthetic data are shown in Figure 4 for the periods of 20, 50, and 100 s. The input model can be largely recovered at all periods except at the lower-left corner where fading and smearing occur due to the insufficient crossing ray paths. Our tests imply that the resolution within seismic array is ~150 km or better at all periods, sufficient to image the anomalies discussed in this study.

3.2. Love Wave Phase Velocity

Love wave phase velocity maps at 20, 25, 30, 34, 40, 45, 50, 59, 71, 77, 91, and 100 s are computed using the phase velocity tomographic inversion method as described in section 3.1. The maps of phase velocity anomaly at the periods of 20, 40, 59, 77, and 100 s are shown in Figures 5a–5e. Figure S1 in the supporting information exhibits the standard error of phase velocity at those periods. These phase velocity maps are clipped by 1% contour of twice the standard errors at 20 s (Figure 5f). Phase velocity anomalies vary gradually with periods due to the overlapped depth sensitivities of neighboring periods (Figure 6a). A continuous low velocity anomaly in the QOB, an area between the Haiyuan fault and the east Kunlun fault, is generally imaged at periods from 20 to 100 s (Figures 5a–5e). The observation of this low velocity anomaly is consistent with previous Rayleigh wave tomography models (Bao, Song, & Li, 2015; Li et al., 2017), while it is partially different from a relatively high velocity in the north QOB obtained from previous Rayleigh and Love wave tomography study (Li et al., 2013, 2016), which has limited station coverage and crossing ray paths there. The Songpan-Ganzi terrane (SGT) is characterized by low velocity anomaly at periods less than 50 s (Figures 5a and 5b) and relatively high velocity compared with the QOB at periods of 59–100 s. Another interesting feature is the sharp velocity contrast between high phase velocities in the Ordos block (OB) and low phase velocities in the Alxa block (AB) at intermediate-long periods (>45 s) (Figures 5c–5e). Our observation is different from the high Rayleigh wave phase and group velocity in the AB from previous Rayleigh wave tomography (Li et al., 2017). Such difference between the Rayleigh and Love wave probably implies the existence of radial anisotropy beneath the AB in the lithospheric mantle.

3.3. SH Wave Velocity

The SH wave velocity model (V_{SH}) is inverted from the Love wave phase velocities at 12 periods ranging from 20 to 100 s at each grid node on the map. Model resolution kernels (rows from the model resolution matrix) corresponding to five layers at depths of roughly 5, 35, 80, 120, and 160 km are plotted in Figure 6b. The resolution is sufficient enough to resolve the average velocity in the targeted layer and its vicinity. For instance, the velocity at 35-km depth might have contributions from the velocity at depths of 20 to 60 km but is not likely affected by velocity at depths below 80 km (Figure 6b). Although the resolution decreases with depth due to the lack of data at long periods (>100 s), the average velocity for each defined layer is well resolved for depths above 130 km. Therefore, we interpret the velocity model above the depth of 130 km. The average V_{SH} (red line in Figure 7b) beneath the study area is well constrained with standard deviation from 0.018 to 0.025 km/s since only one model parameter is solved for each layer in this inversion. The prediction of phase velocities from this 1-D average model well fits the observation (Figure 7a). The 3-D V_{SH} model is constructed using this average V_{SH} as a starting model and perturbing it to fit high-resolution Love wave dispersion maps. The posteriori error value of the final 3-D model is less than 0.03 km/s (~0.8% assuming an average V_{SH} value of 4 km/s) for the entire study region (Figure S2). The error at shallow depths (Figure S2a) is larger than those at other depths (Figures S2b–S2g) due to the lack of Love wave phase velocity at short period (<20 s).

Figures 8 and 9 show seven horizontal and four vertical sections of the SH wave velocity absolute values and perturbations from the 3-D inversion at depths from the surface to 130 km, respectively. Our results in the

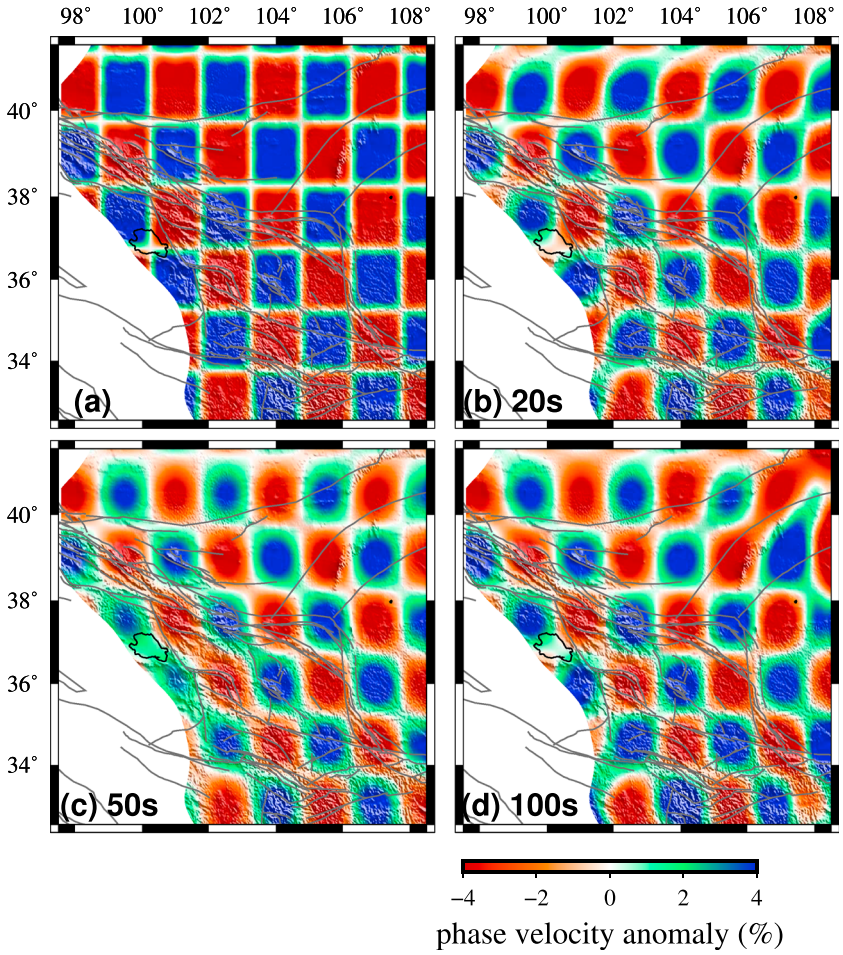

Figure 4. Examples of checkerboard resolution tests. (a) Synthetic checkerboard model. The magnitudes of the input anomalies are 4%, and sizes of anomalies are ~1.5° × 1.5°. (b–d) Retrieved phase velocity at periods 20, 50, and 100 s.

QOB and the SGT largely agree with the previous SH wave velocity model obtained by Li et al. (2016) using the same method but different seismic data from an irregular array with a small number of stations. However, our current V_{SH} model could provide more details on the QOB region with high station coverage compared to the previous V_{SH} model (Li et al., 2016). Low velocities characterize the crust and uppermost mantle beneath the QOB and the SGT (Figures 8 and 9), which is consistent with the slow *P* wave velocity (Li et al., 2008; Lei & Zhao, 2016), slow SV wave velocity from earthquake surface wave tomography (Li et al., 2017) and from joint inversion of receiver functions and Rayleigh wave dispersions (Zheng et al., 2016). Li et al. (2014) also observed middle- to lower-crustal low SV wave velocity in this area from ambient noise tomography.

In order to investigate whether this observed low velocity in the middle-lower crust and uppermost mantle is a robust feature, we performed four synthetic tests. We first built a 1-D V_{SH} model by assigning a low velocity of −5% in middle crust, lower crust, and uppermost mantle, respectively, and subsequently assigning a low velocity of −5% in abovementioned three layers simultaneously, then calculated Love wave phase velocities using the same method to what we used for inversion (Saito, 1988) to recover the given V_{SH} model from the calculated phase velocities (Figure S3). As shown in Figure S3, the inversion can well recover these four input models, though the amplitudes of input and recovered models are not exactly the same. For the input model with lower velocity of −5% in the lower crust, the inversion introduces small vertical smearing in the middle crust and uppermost mantle (Figure S3c), while the small fraction of low velocity is introduced in the upper and lower crust when we assigned −5% lower velocity in the middle crust (Figure S3a). However, the model with lower velocity of −5% in the uppermost mantle would introduce ~2% low

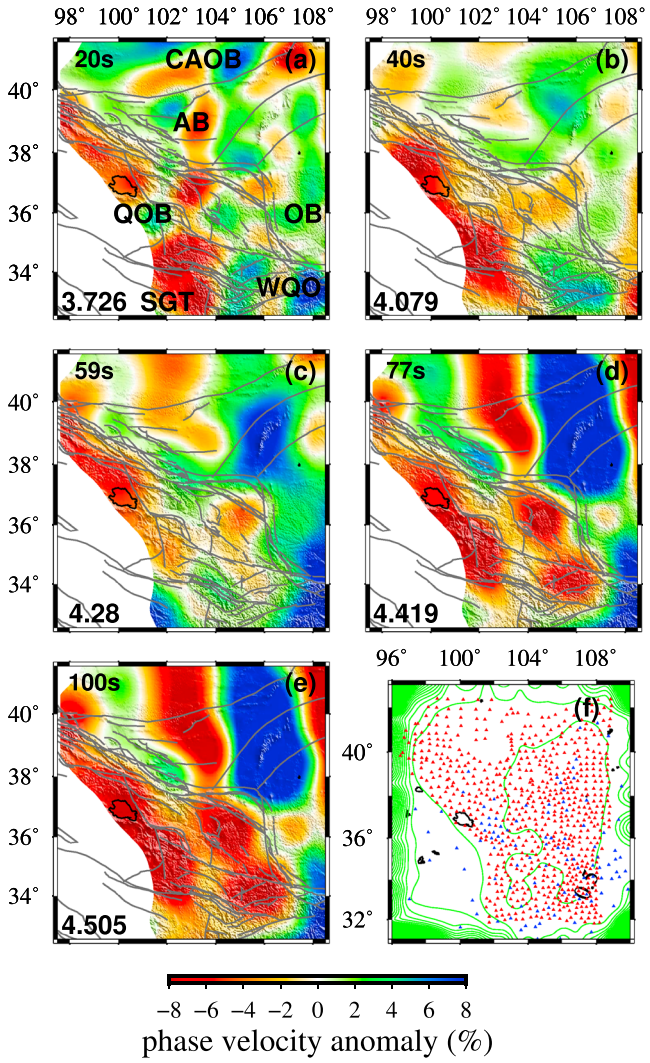

Figure 5. (a–e) Phase velocity perturbations relative to the average phase velocity with the unit of km/s (the lower left corner) at five periods. (f) Uncertainty of the phase velocity at 20 s. The phase velocity maps are clipped by the 1% error contour in Figure 5f. AB = Alxa Block; OB = Ordos Block; CAOB = Central Asian Orogenic Belt; QOB = Qilian orogenic belt; WQO = Western Qinling Orogen.

velocity in the lower crust (Figure S3e). We cannot exclude the possibility that the observed low velocity in the lower crust has a part of contributions from smearing of uppermost mantle low velocity in the inversion. Those artificial features are due to the smoothing applied in the inversion that forces coherent variations between adjacent layers. It is important to note that for abovementioned three input models the artificial feature in the uppermost mantle is not comparable to what we observed. More interestingly, when we assigned the −5% lower velocity in three layers simultaneously, the model can be well recovered (Figure S3g). Generally, these four tests have demonstrated that the observed low velocity in the middle-lower crust and uppermost mantle is a robust feature.

Relatively high velocity anomalies are imaged in the OB (Figures 8, 9e, and 9f) and the western Qinling Orogen (Figures 8, 9a, and 9b) down to 130 km. Such high velocity anomaly is also observed in the regional *P* wave (Li et al., 2008) and SV wave velocity models (Guo & Chen, 2017; Li et al., 2017; Zhang et al., 2011). The fast velocity beneath the OB (Figures 8, 9e, and 9f) could indicate that this region is old and cold (Hu et al., 2000). A low velocity with an elongated shape is observed at depths of 25–130 km beneath the central AB and the Central Asian Orogenic Belt (Figures 8c–8g and 9e–9h). This is consistent with slow *P* wave velocity in the upper mantle (Li et al., 2008) but does not agree with the SV wave velocity model that imaged a high velocity anomaly at the depths of 30–90 km (Li et al., 2017). Such discrepancy between our model and the previous V_{SV} model could result from either different methods or the presence of radial anisotropy in this area, which need further investigation.

4. Discussion

4.1. Crustal Low Velocity Zones Beneath the NE Tibetan Plateau

Our tomographic images reveal widespread low SH wave velocity zones (Figures 8a–8c and 9) in the crust beneath the NE Tibetan plateau, specifically in the QOB and SGT regions. Such slow V_{SH} is also observed in the lower crust of the southeastern Tibetan plateau (Fu et al., 2017), which is interpreted as an indicator of lower crustal flow. SV wave velocity obtained from Rayleigh wave ambient noise tomography indicated that the midlower crustal low velocity zones distribute across most of the Tibetan plateau (Jiang et al., 2011; Li et al., 2014; Yang et al., 2012). These slow velocity zones usually exhibit high electrical conductivity (Bai et al., 2010; Unsworth et al., 2005; Wei et al., 2001; Xiao et al., 2013), implying a weak and partial molten midlower crust. Yang et al. (2012) suggested that both the partial melt and radial anisotropy due to horizontal alignment of crustal anisotropic minerals (e.g., micas and amphibolites) could contribute to the observed low SV wave speed and the effect of mineral alignment would significantly reduce the need for partial melt. Here the slow V_{SV} (Li et al., 2017) and V_{SH} from our inversion as well as positive radial anisotropy ($V_{SH} > V_{SV}$; Li et al., 2016) in the midlower crust beneath the QOB and northern SGT (Figures 8b, 8c, and 9) may also imply that a horizontal melt-rich layer likely exists in the NE Tibetan plateau. This horizontal melt-rich layer could result in strong crustal azimuthal anisotropy inferred from receiver function analysis (Shen, Yuan, & Ren, 2015) and shear wave splitting measurement (Li et al., 2011) and correlates well with relatively low-resistivity (Xiao et al., 2013) and high Lg-wave attenuation belt (Zhao et al., 2013) in the lower crust and relatively high surface heat flow (Zhang et al., 2018).

Though partial melt is suggested to have occurred in the NE Tibetan plateau, it is not yet known if these low velocity zones are sufficiently weak and interconnected to enable regional-scale channel flow. Our tomographic images suggest substantial lateral heterogeneity of the amplitude of these zones but have

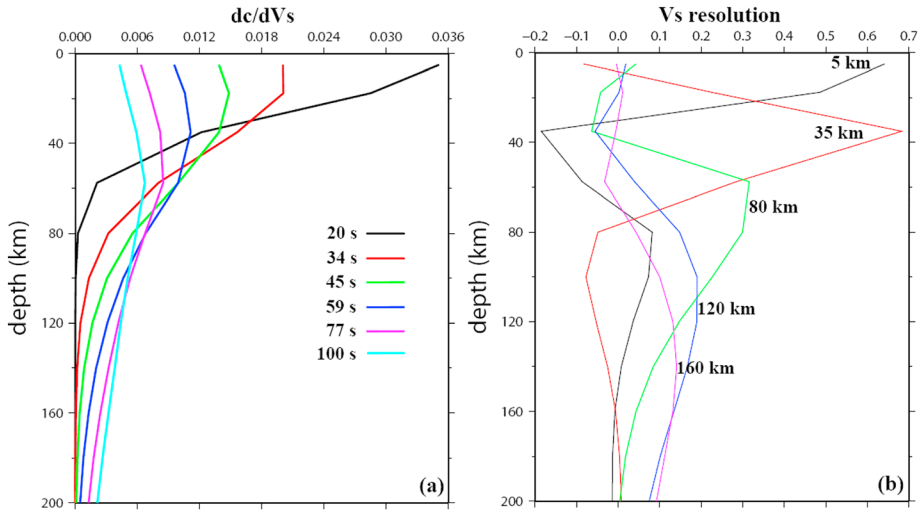

Figure 6. (a) Phase velocity sensitivity kernel at six periods based on the AK135 model. (b) Depth resolution of shear wave velocity from the model resolution matrix.

difficulties in determining how much wave speed reduction in the midlower crust could induce flow. Numerical modeling is required to identify regions in which channel flow may occur.

4.2. Mechanisms of Uplift in the NE Tibetan Plateau

The NE Tibetan plateau is characterized with an average elevation of ~4.5 km and rapidly drops off to <1.5 km toward the northeast. Previous studies suggested that the high elevation of the Tibetan plateau could be formed and maintained through four modes, that is, upper crustal thickening (e.g., Houseman & England, 1993; Kind et al., 2002), midlower crustal flow, thermal buoyancy of lithospheric mantle (England & Houseman, 1989; Jimenez-Munt & Platt, 2006; Molnar et al., 1993; Tseng et al., 2009), and extrusive rigid block (Tapponnier et al., 2001). Though a large amount of studies has been conducted in the NE Tibetan plateau in an attempt to distinguish these models, which modes of

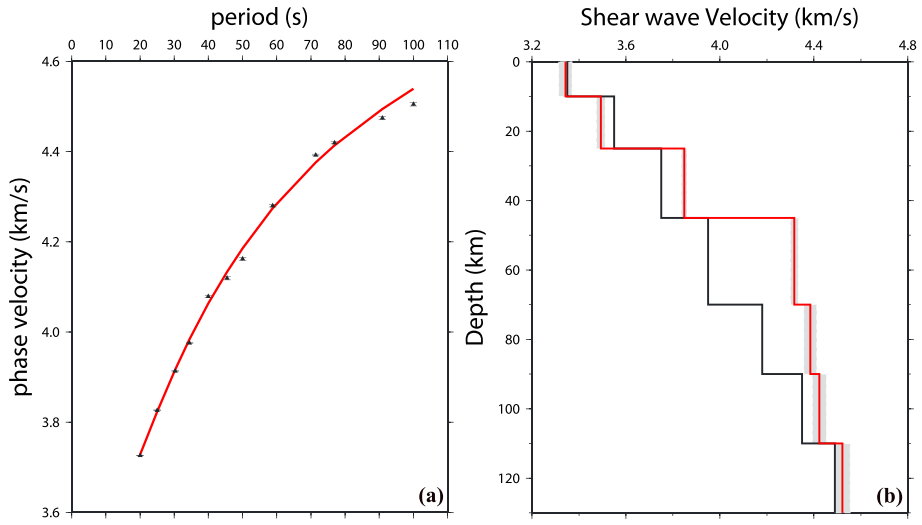

Figure 7. (a) Observed and predicted average Love wave phase velocities. The triangles are the observed dispersion data with two standard deviations indicated by the error bars. The predicted from the best fitting models in (b) is shown as red line. (b) Shear wave velocity models. The black line is the modified AK135 model used as an initial model for the inversion. The red line is the best fitting model. The width of the shaded area shows the standard error of shear wave velocity in each layer.

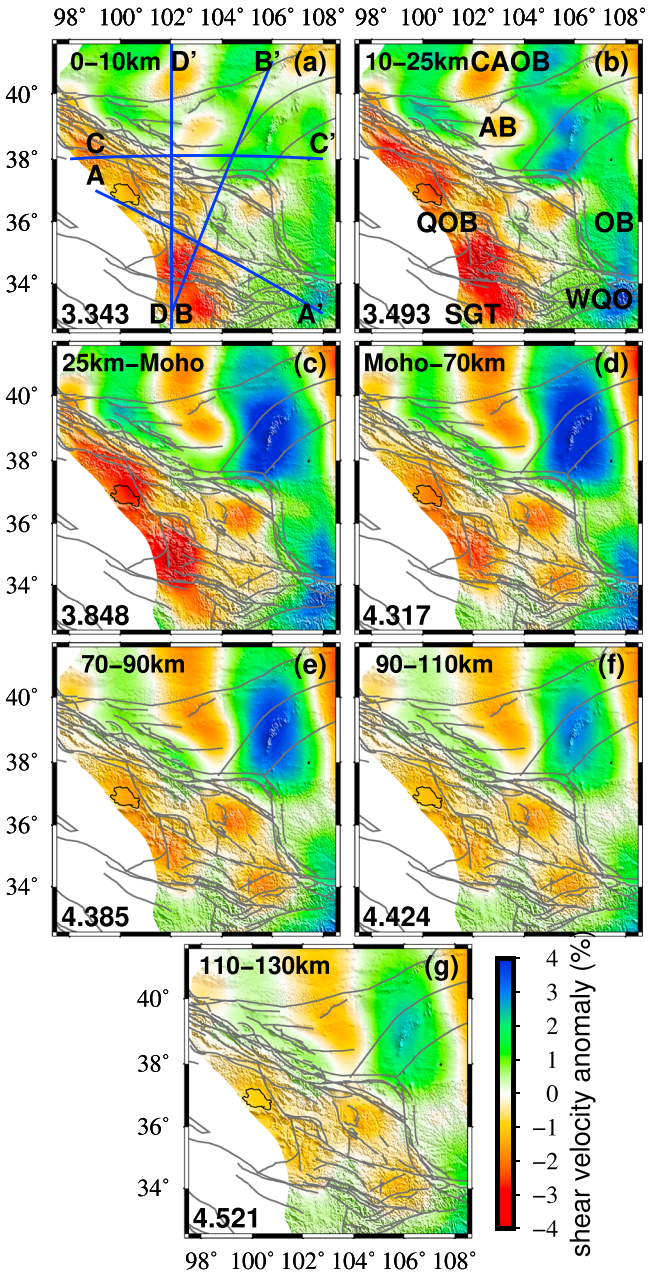

Figure 8. Horizontal slices of shear wave velocity structure in the crust and uppermost mantle. The anomaly is relative to the average velocity with the unit of km/s marked in the lower left corner. AB = Alxa Block; OB = Ordos Block; CAOB = Central Asian Orogenic Belt; QOB = Qilian orogenic belt; WQO = Western Qinling Orogen; SGT = Songpan-Ganzi terrane.

deformation dominates and is responsible for the current elevation remain unclear and still a long-lasting debate. For example, Lease et al. (2012) suggested that pure shear alone may account for the Cenozoic crustal thickening in northeastern Tibet, which may obviate lower crustal flow as a necessary crustal thickening agent. While some studies argued the removal of some or all of the mantle lithosphere occurred beneath the NE Tibetan plateau (e.g., Li et al., 2013, 2016, 2017; Molnar et al., 1993), offering a sensible explanation for the change in orientation of deformation in NE Tibetan plateau (Yuan et al., 2013). Several lines of geologic evidence support that the modern extent of Cenozoic deformation and high topography along the NE Tibetan plateau was established during the late Miocene (Wang et al., 2017; Yuan et al., 2013). Magnetostratigraphic study even suggested that significant tectonic uplift occurred as late as Pliocene (Pares et al., 2003). All these indicate that the NE plateau is still in the early stage of uplift and deformation (Meyer et al., 1998; Tapponnier et al., 2001). We speculated that no single model can explain the high elevations of the northeastern plateau given the complex uplift history of northeast Tibet.

In our 3-D V_{SH} model, a low velocity anomaly is observed in the mid-lower crust and can be traced down to uppermost mantle beneath the QOB (Figures 8d–8g and 9), consistent with the observations of slow *P* wave velocity (Lei & Zhao, 2016) and SV wave velocity (Li et al., 2013, 2017), and inefficient propagation of high frequency Sn (Barron & Priestley, 2009). Additionally, a diffuse lithosphere asthenosphere boundary from S receiver function suggests small temperature gradient between mantle lithosphere and asthenosphere (Shen, Yuan, & Liu, 2015). These facts could indicate that the sub-Moho upper mantle is weak and hot. This hot uppermost mantle could result from radioactive heating from the thickened crust (McKenzie & Priestley, 2008), which could be at least 45 km due to the shortening before the Middle Miocene (Lease et al., 2012). We cannot rule out that the crustal radioactivity would partly lower the uppermost mantle velocity. However, given the velocity value of ~4.2 km/s in the uppermost mantle (Moho —120 km), a different process may also be responsible for the low velocity. Alternatively, the hot uppermost mantle beneath the QOB could be attributed to asthenosphere upwelling after lithospheric mantle removal in the NE Tibetan plateau, consistent with the interpretation of recent surface wave studies (Li et al., 2013, 2016, 2017; Zheng et al., 2016). In this scenario, we speculate that thermal isostasy in the mantle partially contributes to the uplift due to the high temperature and strong positive buoyancy. Hasterok and Chapman (2007) demonstrated that thermal isostasy in continental regions can produce nearly 3 km of relief, comparable to thermal elevation differences between young and old oceanic crust. Therefore, deep-seated thermal buoyancy after lithospheric delamination could contribute a portion of high topography in the NE Tibetan plateau and asthenosphere upwelling could explain the occurrence of partial melting in the mid-lower crust.

4.3. High Velocity Anomaly in the Lithosphere Beneath the Qinling Orogen

Clark and Royden (2000) suggested that the southwestern Qinling could act as a corridor for the lower crustal flow due to its relatively weak structure of the Paleozoic-Mesozoic Qinling suture bounded by the rheologically strong Sichuan basin along the Longmen Shan and the Ordos block along the Liupan Shan. The

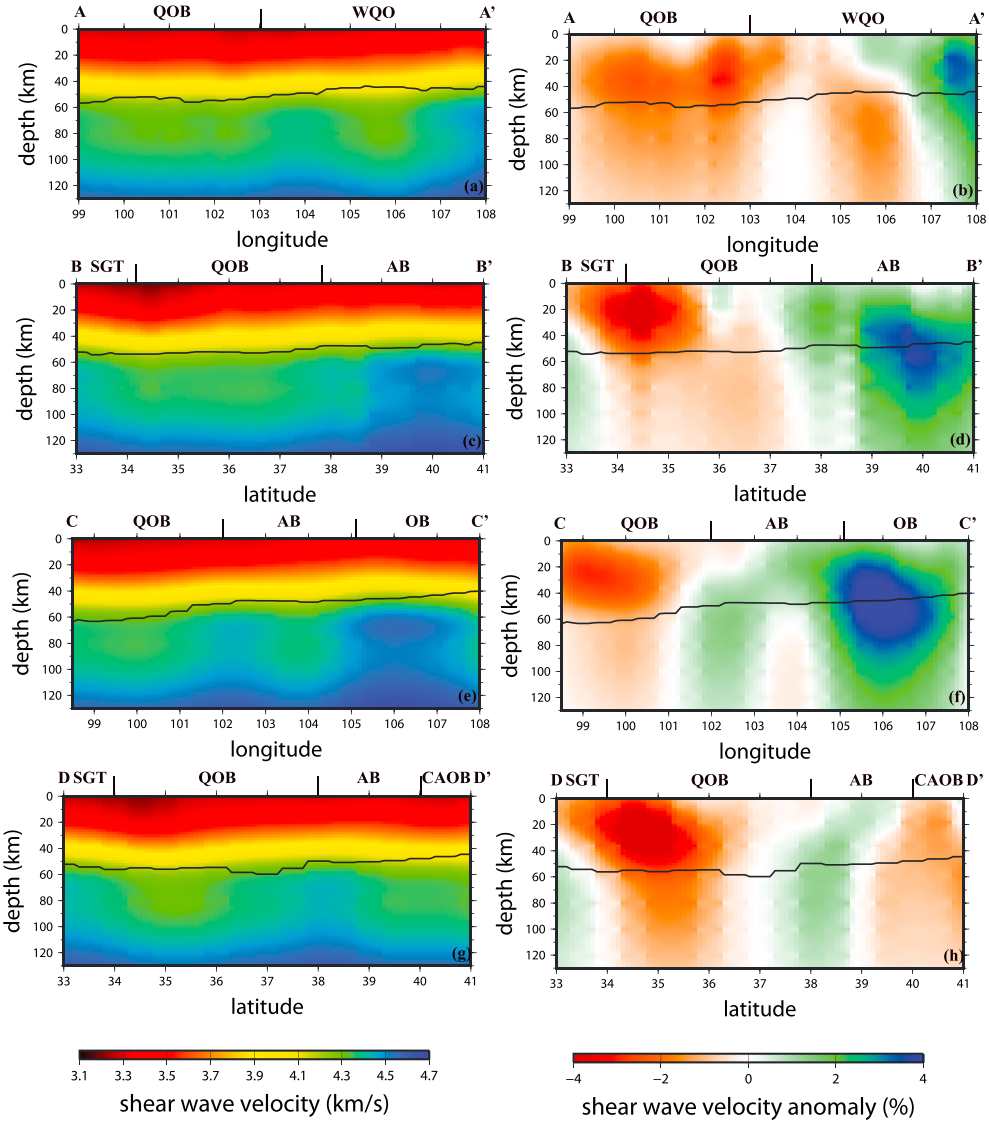

Figure 9. Vertical slices of the absolute shear wave velocity (a, c, e, and g) and velocity anomaly (b, d, f, and h) along four profiles with locations shown in Figure 8a. AB = Alxa Block; OB = Ordos Block; CAOB = Central Asian Orogenic Belt; QOB = Qilian orogenic belt; WQO = Western Qinling Orogen; SGT = Songpan-Ganzi terrane.

thermochronologic data in the Qinling Orogen fit the predicted surface uplift, exhumation, and deformation from this lower crustal flow model (Enkelmann et al., 2006). If the lower crustal channel flow exists beneath the Qinling Orogen, the observation of low velocity should be expected in the lower crust. However, our SH wave velocity model exhibits fast velocity anomaly in most of lithosphere beneath the western Qinling Orogen (Figures 8a–8c, 9a, and 9b), which is contradictory to the nature of the eastward crustal flow model. Additionally, the absence of significantly slow SV wave velocity (Guo & Chen, 2007; Li et al., 2017) and the intermediate-low V_P/V_S (< 1.8) in the lower crust (Ye et al., 2017), indicative of an intermediate to felsic composition, also imply that the lower crust of the Qinling Orogen is not currently serving as a channel accommodating the extrusion of the Tibetan plateau material (Ye et al., 2017). Instead of the crustal flow, the asthenospheric flow likely exists beneath the Qinling Orogen, as supported by previous studies from *P* wave traveltime tomography (Li & van der Hilst, 2010), teleseismic shear wave splitting measurement (Soto et al., 2012), and Rayleigh wave tomography (Zhang et al., 2011), to accommodate eastward escape of the Tibetan plateau material toward eastern China. A radial anisotropy model from discrepancies of Rayleigh and Love wave phase velocities at longer periods could be used to test this hypothesis, but it is beyond the scope of this paper.

5. Conclusions

In this study, we construct a high-resolution isotropic SH wave velocity model down to ~130 km by inverting the fundamental-mode Love waves from the dense ChinArray II and China Digital Seismic Array seismic array for periods between 20 and 100 s in the northeastern Tibetan plateau and its adjacent regions. Our model reveals widespread low wave speed zones in the midlower crust of the NE Tibetan plateau. The reduced shear wave speed could be attributed to partial melts in the crust. Slow SH wave velocity is also observed in the uppermost mantle, indicating a warm and weak lithosphere in the NE Tibetan plateau. This slow velocity could result from asthenosphere upwelling after lithospheric mantle removal in this region. The consequence of the asthenosphere upwelling is the occurrence of partial melting in the midlower crust and a portion of high topography in this region via deep-seated thermal buoyancy after delamination. Fast SH wave velocity appears in the western Qinling Orogen from the surface to the depth of 130 km, implying that the lower crustal channel flow model probably does not work in this region.

Acknowledgments
The data was provided by China Seismic Array Data Management Center at Institute of Geophysics, China Earthquake Administration. The velocity model and Love wave waveform can be downloaded from https://osf.io/pqxnw/?view_only=6eae98b48791433a91378e1ea383194d website. We thank the participants in the ChinArray II for collecting the data. Editor Martha Savage, Associate Editor, and three anonymous reviewers provided useful suggestions and comments on the manuscript. Most figures were made with General Mapping Tools (Wessel & Smith, 1998). This work was supported by National Science Foundation of China (41574042 and 41804043), the basic research project of Institute of Earthquake Forecasting, CEA (2018IEF0302 and 2017IES0402), and the Second Tibetan Plateau Scientific Expedition and Research Program (grant no. 2019QZKK0701).

References

Bai, D., Unsworth, M. J., Meju, M. A., Ma, X., Teng, J., Kong, X., et al. (2010). Crustal deformation of the eastern Tibetan Plateau revealed by magnetotelluric imaging. *Nature Geoscience*, *3*(5), 358–362. https://doi.org/10.1038/ngeo830

Bao, X., Song, X., & Li, J. (2015). High-resolution lithospheric structure beneath Mainland China from ambient noise and earthquake surface-wave tomography. *Earth and Planetary Science Letters*, *417*, 132–141. https://doi.org/10.1016/j.epsl.2015.02.024

Bao, X., Song, X., Xu, M., Wang, L., Sun, X., Mi, N., et al. (2013). Crust and upper mantle structure of the North China Craton and the NE Tibetan Plateau and its tectonic implications. *Earth and Planetary Science Letters*, *369-370*, 129–137. https://doi.org/10.1016/j.epsl.2013.03.015

Bao, X., Sun, X., Xu, M., Eaton, D. W., Song, X., Wang, L., et al. (2015). Two crustal low-velocity channels beneath SE Tibet revealed by joint inversion of Rayleigh wave dispersion and receiver functions. *Earth and Planetary Science Letters*, *415*, 16–24. https://doi.org/10.1016/j.epsl.2015.01.020

Barron, J., & Priestley, K. (2009). Observations of frequency-dependent S n propagation in Northern Tibet. *Geophysical Journal International*, *179*(1), 475–488.

Beaumont, C., Jamieson, R. A., Nguyen, M. H., & Lee, B. (2001). Himalayan tectonics explained by extrusion of a low-viscosity channel coupled to focused surface denudation. *Nature*, *414*(6865), 738–742. https://doi.org/10.1038/414738a

Beck, R. A., Burbank, D. W., Sercombe, W. J., Riley, G. W., Barndt, J. K., Berry, J. R., et al. (1995). Stratigraphic evidence for an early collision between northwest India and Asia. *Nature*, *373*(6509), 55–58. https://doi.org/10.1038/373055a0

Bird, P. (1991). Lateral extrusion of lower crust from under high topography, in the isostatic limit. *Journal of Geophysical Research*, *96*(B6), 10,275–10,286. https://doi.org/10.1029/91JB00370

Chen, Z., Burchfiel, B. C., Liu, Y., King, R. W., Royden, L. H., Tang, W., et al. (2000). GPS measurements from eastern Tibet and their implications for India/Eurasia intracontinental deformation. *Journal of Geophysical Research*, *105*(B7), 16,215–16,227. https://doi.org/10.1029/2000JB900092

Clark, M. K., Bush, J. W. M., & Royden, L. H. (2005). Dynamic topography produced by lower crustal flow against rheological strength heterogeneities bordering the Tibetan Plateau. *Geophysical Journal International*, *162*(2), 575–590. https://doi.org/10.1111/j.1365-246X.2005.02580.x

Clark, M. K., & Royden, L. H. (2000). Topographic ooze: building the eastern margin of Tibet by lower crustal flow. *Geology*, *28*(8), 703–709. https://doi.org/10.1130/0091-7613(2000)28<703:TOBTEM>2.0.CO;2

Duret, F., Shapiro, N. M., Cao, Z., Levin, V., Molnar, P., & Roecker, S. (2010). Surface wave dispersion across Tibet: Direct evidence for radial anisotropy in the crust. *Geophysical Research Letters*, *37*, L16306. https://doi.org/10.1029/2010GL043811

England, P. C., & Houseman, G. A. (1989). Extension during continental convergence, with application to the Tibetan plateau. *Journal of Geophysical Research*, *94*(B12), 17,561–17,579. https://doi.org/10.1029/JB094iB12p17561

Enkelmann, E., Ratschbacher, L., Jonckheere, R., Nestler, R., Fleischer, M., Gloaguen, R., et al. (2006). Cenozoic exhumation and deformation of northeastern Tibet and the Qinling: Is Tibetan lower crustal flow diverging around the Sichuan Basin? *Geological Society of America Bulletin*, *118*(5-6), 651–671. https://doi.org/10.1130/B25805.1

Fielding, E., Isacks, B., Barazangi, M., & Duncan, C. (1994). How flat is Tibet. *Geology*, *22*(2), 163–167. https://doi.org/10.1130/0091-7613(1994)022<0163:HFIT>2.3.CO;2

Fu, Y. V., Gao, Y., Li, A., Li, L., & Chen, A. (2017). Lithospheric structure of the southeastern margin of the Tibetan Plateau from Rayleigh wave tomography. *Journal of Geophysical Research: Solid Earth*, *122*, 4631–4644.

Gao, R., Wang, H., Yin, A., Dong, S., Kuang, Z., Zuza, A. V., & Xiong, X. (2013). Tectonic development of the northeastern Tibetan Plateau as constrained by high-resolution deep seismic-reflection data. *Lithosphere*, *5*(6), 555–574. https://doi.org/10.1130/L293.1

Guo, Z., & Chen, Y. J. (2017). Mountain building at northeastern boundary of Tibetan Plateau and craton reworking at Ordos block from joint inversion of ambient noise tomography and receiver functions. *Earth and Planetary Science Letters*, *463*, 232–242. https://doi.org/10.1016/j.epsl.2017.01.026

Hasterok, D., & Chapman, D. S. (2007). Continental thermal isostasy: 1. Methods and sensitivity. *Journal of Geophysical Research*, *112*, B06414. https://doi.org/10.1029/2006JB004663

Houseman, G., & England, P. C. (1993). Crustal thickening versus lateral expulsion in the Indian-Asian continental collision. *Journal of Geophysical Research*, *98*(B7), 12,233–12,249. https://doi.org/10.1029/93JB00443

Hu, S., He, L., & Wang, J. (2000). Heat flow in the continental area of China: A new data set. *Earth and Planetary Science Letters*, *179*(2), 407–419. https://doi.org/10.1016/S0012-821X(00)00126-6

Huang, Z., Wang, P., Xu, M., Wang, L., Ding, Z., Wu, Y., et al. (2015). Mantle structure and dynamics beneath SE Tibet revealed by new seismic images. *Earth and Planetary Science Letters*, *411*, 100–111. https://doi.org/10.1016/j.epsl.2014.11.040

Jiang, M., Zhou, S., Sandvol, E., Chen, X., Liang, X., Chen, Y. J., & Fan, W. (2011). 3-D lithospheric structure beneath southern Tibet from Rayleigh-wave tomography with a 2-D seismic array. *Geophysical Journal International*, *185*(2), 593–608.

Jimenez-Munt, I., Fernandez, M., Verges, J., & Platt, J. P. (2008). Lithosphere structure underneath the Tibetan Plateau inferred from elevation, gravity and geoid anomalies. *Earth and Planetary Science Letters*, *267*(1-2), 276–289. https://doi.org/10.1016/j.epsl.2007.11.045

Jimenez-Munt, I., & Platt, J. P. (2006). Influence of mantle dynamics on the topographic evolution of the Tibetan Plateau: Results from numerical modeling. *Tectonics*, *25*, TC6002. https://doi.org/10.1029/2006TC001963

Kind, R., Yuan, X., Saul, J., Nelson, D., Sobolev, S. V., & Mechie, J. (2002). Seismic images of crust and upper mantle beneath Tibet: Evidence for Eurasian plate subduction. *Science*, *298*(5596), 1219–1221. https://doi.org/10.1126/science.1078115

Lease, R. O., Burbank, D. W., Zhang, H., Liu, J., & Yuan, D. (2012). Cenozoic shortening budget for the northeastern edge of the Tibetan Plateau: Is lower crustal flow necessary? *Tectonics*, *31*, TC3011. https://doi.org/10.1029/2011TC003066

Lei, J., & Zhao, D. (2016). Teleseismic *P*-wave tomography and mantle dynamics beneath Eastern Tibet. *Geochemistry, Geophysics, Geosystems*, *17*, 1861–1884. https://doi.org/10.1002/2016GC006262

Li, A., & Li, L. (2015). Love wave tomography in southern Africa from a two-plane wave inversion method. *Geophysical Journal International*, *202*(2), 1005–1020. https://doi.org/10.1093/gji/ggv203

Li, C., & van der Hilst, R. D. (2010). Structure of the upper mantle and transition zone beneath southeast Asia from traveltime tomography. *Journal of Geophysical Research*, *115*, B07308. https://doi.org/10.1029/2009JB006882

Li, C., van der Hilst, R. D., Meltzer, A. S., & Engdahl, E. R. (2008). Subduction of the Indian lithosphere beneath the Tibetan Plateau and Burma. *Earth and Planetary Science Letters*, *274*(1-2), 157–168. https://doi.org/10.1016/j.epsl.2008.07.016

Li, H., Shen, Y., Huang, Z., Li, X., Gong, M., Shi, D., et al. (2014). The distribution of the mid-to-lower crustal low-velocity zone beneath the northeastern Tibetan Plateau revealed from ambient noise tomography. *Journal of Geophysical Research: Solid Earth*, *119*, 1954–1970. https://doi.org/10.1002/2013JB010374

Li, L., Li, A., Murphy, M. A., & Fu, Y. V. (2016). Radial anisotropy beneath northeast Tibet, implications for lithosphere deformation at a restraining bend in the Kunlun fault and its vicinity. *Geochemistry, Geophysics, Geosystems*, *17*, 3674–3690. https://doi.org/10.1002/2016GC006366

Li, L., Li, A., Shen, Y., Sandvol, E. A., Shi, D., Li, H., & Li, X. (2013). Shear wave structure in the northeastern Tibetan Plateau from Rayleigh wave tomography. *Journal of Geophysical Research: Solid Earth*, *118*, 4170–4183. https://doi.org/10.1002/jgrb.50292

Li, Y., Pan, J., Wu, Q., & Ding, Z. (2017). Lithospheric structure beneath the northeastern Tibetan Plateau and the western Sino-Korea Craton revealed by Rayleigh wave tomography. *Geophysical Journal International*, *210*(2), 570–584. https://doi.org/10.1093/gji/ggx181

Li, Y., Wu, Q., Zhang, F., Feng, Q., & Zhang, R. (2011). Seismic anisotropy of the northeastern Tibetan Plateau from shear wave splitting analysis. *Earth and Planetary Science Letters*, *304*(1-2), 147–157. https://doi.org/10.1016/j.epsl.2011.01.026

Liang, S., Gan, W., Shen, C., Xiao, G., Liu, J., Chen, W., et al. (2013). Three-dimensional velocity field of present-day crustal motion of the Tibetan Plateau derived from GPS measurements. *Journal of Geophysical Research: Solid Earth*, *118*, 5722–5732. https://doi.org/10.1002/2013JB010503

McKenzie, D., & Priestley, K. (2008). The influence of lithospheric thickness variations on continental evolution. *Lithos*, *102*(1-2), 1–11. https://doi.org/10.1016/j.lithos.2007.05.005

Métivier, F., Gaudemer, Y., Tapponnier, P., & Meyer, B. (1998). Northeastward growth of the Tibet plateau deduced from balanced reconstruction of two depositional areas: The Qaidam and Hexi Corridor basins, China. *Tectonics*, *17*(6), 823–842.

Meyer, B., Tapponnier, P., Bourjot, L., Métivier, F., Gaudemer, Y., Peltzer, G., Shunmin, G., & Zhitai, C. (1998). Crustal thickening in Gansu-Qinghai, lithospheric mantle subduction, and oblique, strike-slip controlled growth of the Tibet plateau. *Geophysical Journal International*, *135*(1), 1–47.

Molnar, P., England, P. C., & Martinod, J. (1993). Mantle dynamics, uplift of the Tibetan Plateau and the Indian monsoon. *Reviews of Geophysics*, *31*(4), 357–396. https://doi.org/10.1029/93RG02030

Pan, S., & Niu, F. (2011). Large contrasts in crustal structure and composition between the Ordos plateau and the NE Tibetan plateau from receiver function analysis. *Earth and Planetary Science Letters*, *303*(3-4), 291–298. https://doi.org/10.1016/j.epsl.2011.01.007

Pares, J. M., van der Voo, R., Downs, W. R., & Yan, M. (2003). Northeastward growth and uplift of the Tibetan Plateau: Magnetostratigraphic insights from the Guide Basin. *Journal of Geophysical Research*, *108*(B8), 2400. https://doi.org/10.1029/2003JB002624

Saito, M. (1988). DISPER80: a subroutine package for the calculation of seismic normal-mode solutions. In D. J. Doornbos (Ed.), *Seismological Algorithms: Computational Methods and Computer Programs* (pp. 293–319). New York: Elsevier.

Schoenbohm, L. M., Burchfiel, B. C., & Chen, L. (2006). Propagation of surface uplift, lower crustal flow, and Cenozoic tectonics of the southeast margin of the Tibetan Plateau. *Geology*, *34*(10), 813–816. https://doi.org/10.1130/G22679.1

Shapiro, N. M., Ritzwoller, M. H., Molnar, P., & Levin, V. (2004). Thinning and flow of Tibetan crust constrained by seismic anisotropy. *Science*, *305*(5681), 233–236. https://doi.org/10.1126/science.1098276

Shen, X., Yuan, X., & Liu, M. (2015). Is the Asian lithosphere underthrusting beneath northeastern Tibetan Plateau? Insights from seismic receiver functions. *Earth and Planetary Science Letters*, *428*, 172–180. https://doi.org/10.1016/j.epsl.2015.07.041

Shen, X., Yuan, X., & Ren, J. (2015). Anisotropic low-velocity lower crust beneath the northeastern margin of Tibetan Plateau: Evidence for crustal channel flow. *Geochemistry, Geophysics, Geosystems*, *16*, 4223–4236. https://doi.org/10.1002/2015GC005952

Soto, G. L., Sandvol, E., Ni, J. F., Flesch, L., Hearn, T. M., Tilmann, F., et al. (2012). Significant and vertically coherent seismic anisotropy beneath eastern Tibet. *Journal of Geophysical Research*, *117*, B05308. https://doi.org/10.1029/2011JB008919

Tapponnier, P., Xu, Z., Roger, F., Meyer, B., Arnaud, N., Wittlinger, G., & Yang, J. (2001). Oblique stepwise rise and growth of the Tibet Plateau. *Science*, *294*(5547), 1671–1677. https://doi.org/10.1126/science.105978

Tarantola, A., & Valette, B. (1982). Generalized non-linear problems solved using the least-squares criterion. *Reviews of Geophysics*, *20*(2), 219–232. https://doi.org/10.1029/RG020i002p00219

Tseng, T., Chen, W., & Nowack, R. L. (2009). Northward thinning of Tibetan crust revealed by virtual seismic profiles. *Geophysical Research Letters*, *36*, L24304. https://doi.org/10.1029/2009GL040457

Unsworth, M. J., Jones, A. G., Wei, W., Marquis, G., Gokarn, S. G., Spratt, J. E., & the INDEPTH-MT Team (2005). Crustal rheology of the Himalaya and southern Tibet inferred from magnetotelluric data. *Nature*, *438*(7064), 78–81. https://doi.org/10.1038/nature04154

Wang, Q., Niu, F., Gao, Y., & Chen, Y. (2016). Crustal structure and deformation beneath the NE margin of the Tibetan plateau constrained by teleseismic receiver function data. *Geophysical Journal International*, *204*(1), 167–179. https://doi.org/10.1093/gji/ggv420

Wang, W., Wu, J., Fang, L., Lai, G., & Cai, Y. (2017). Sedimentary and crustal thicknesses and Poisson's ratios for the NE Tibetan Plateau and its adjacent regions based on dense seismic arrays. *Earth and Planetary Science Letters*, *462*, 76–85. https://doi.org/10.1016/j.epsl.2016.12.040

Wei, W., Unsworth, M., Jones, A., Booker, J., Tan, H., Nelson, D., et al. (2001). Detection of widespread fluids in the Tibetan crust by Magnetotelluric studies. *Science*, *292*(5517), 716–719. https://doi.org/10.1126/science.1010580

Wessel, P., & Smith, W. H. (1998). New, improved version of Generic Mapping Tools released. *Eos, Transactions American Geophysical Union*, *79*(47), 579. https://doi.org/10.1029/98EO00426

Xiao, Q., Zhang, J., Zhao, G., & Wang, J. (2013). Electrical resistivity structures northeast of the Eastern Kunlun fault in the northeastern Tibet: Tectonic implications. *Tectonophysics*, *601*, 125–138. https://doi.org/10.1016/j.tecto.2013.05.003

Xie, J., Ritzwoller, M. H., Shen, W., Yang, Y., Zheng, Y., & Zhou, L. (2013). Crustal radial anisotropy across Eastern Tibet and the Western Yang-tze Craton. *Journal of Geophysical Research: Solid Earth*, *118*, 4226–4252. https://doi.org/10.1002/jgrb.50296

Xu, L., Rondenay, S., & van der Hilst, R. D. (2007). Structure of the crust beneath the Southeastern Tibetan plateau from teleseismic receiver functions. *Physics of the Earth and Planetary Interiors*, *165*(3-4), 176–193. https://doi.org/10.1016/j.pepi.2007.09.002

Xu, Q., Zhao, J., Pei, S., & Liu, H. (2013). Distinct lateral contrast of the crust and upper mantle structure beneath northeast Tibetan plateau from receiver function analysis. *Physics of the Earth and Planetary Interiors*, *217*, 1–9. https://doi.org/10.1016/j.pepi.2013.01.005

Yang, Y., Ritzwoller, M. H., Zheng, Y., Shen, W., Levshin, A. L., & Xie, Z. (2012). A synoptic view of the distribution and connectivity of the mid-crustal low velocity zone beneath Tibet. *Journal of Geophysical Research*, *117*, B04303. https://doi.org/10.1029/2011JB008810

Ye, Z., Li, J., Gao, R., Song, X., Li, Q., Li, Y., et al. (2017). Crustal and uppermost mantle structure across the Tibet-Qinling transition zone in NE Tibet: Implications for material extrusion beneath the Tibetan plateau. *Geophysical Research Letters*, *44*, 10,316–10,323. https://doi.org/10.1002/2017GL075141

Yin, A., & Harrison, T. M. (2000). Geologic evolution of the Himalayan-Tibetan orogeny. *Annual Review of Earth and Planetary Sciences*, *28*(1), 211–280. https://doi.org/10.1146/annurev.earth.28.1.211

Yuan, D. Y., Ge, W. P., Chen, Z. W., Li, C. Y., Wang, Z. C., Zhang, H. P., et al. (2013). The growth of northeastern Tibet and its relevance to large-scale continental geodynamics: A review of recent studies. *Tectonics*, *32*, 1358–1370. https://doi.org/10.1002/tect.20081

Zhang, C., Shi, Q., & Zhang, L. (2018). Discussion on the relationship between Cenozoic magmatic activity and geotherm in Tibetan Plateau. *Geological Survey of China*, *5*(2), 18–24.

Zhang, Q., Sandvol, E., Ni, J., Yang, Y., & Chen, Y. J. (2011). Rayleigh wave tomography of the northeastern margin of the Tibetan Plateau. *Earth and Planetary Science Letters*, *304*, 103–112.

Zhao, L., Xie, X., He, J., Tian, X., & Yao, Z. (2013). Crustal flow pattern beneath the Tibetan Plateau constrained by regional Lg-wave Q tomography. *Earth and Planetary Science Letters*, *383*, 113–122. https://doi.org/10.1016/j.epsl.2013.09.038

Zheng, D., Li, H., Shen, Y., Tan, J., Ouyang, L., & Li, X. (2016). Crustal and upper mantle structure beneath the northeastern Tibetan Plateau from joint analysis of receiver functions and Rayleigh wave dispersions. *Geophysical Journal International*, *204*(1), 583–590. https://doi.org/10.1093/gji/ggv469